Microstructural characterization and solidification behavior of atomized Al–Fe powders

Y. Zhou
Department of Chemical Engineering and Materials Science, University of California, Irvine, California 92717-2575

J. A. Juarez-Islas and O. Alvarez-Fregoso
Instituto de Investigaciones en Materiales, UNAM, Mexico, D.F., 04510, Mexico

W. Y. Yoon
Department of Metallurgical Engineering, Korea University, Seoul, 136-701, Korea

E. J. Lavernia
Department of Chemical Engineering and Materials Science, University of California, Irvine, California 92717-2575

(Received 1 December 1997; accepted 11 July 1998)

The effect of solidification history on the resultant microstructure in atomized Al–2.56 wt% Fe and Al–6.0 wt% Fe powders was studied, with particular emphasis on droplet size, undercooling, and phase stability. The atomized Al–Fe powders exhibited four microstructural features, i.e., Al_3Fe phase (now known as $Al_{13}Fe_4$), Al + Al_6Fe, α–Al dendrite, and a predendritic microstructure. The presence of these phases was noted to depend on alloy composition and a kinetic phase competitive growth mechanism due to the initial undercooling experienced by the powders. The occurrence of structures of the predendritic, cellular, and/or dendritic type was properly predicted by the theory of dendrite growth into undercooled alloy melts for the case of large undercoolings.

I. INTRODUCTION

The extent of undercooling during solidification of metals plays a critical role in microstructural evolution by dictating phase selection. There are two general approaches that may be effectively utilized to enhance (the degree of) the undercooling, i.e., reducing the potency of heterogeneous nucleants or extracting thermal energy at a rate that is sufficiently high to delay crystallization of the undercooled liquid. The first approach involves the progressive elimination or isolation of potential catalysts.[1–3] The second approach is generally associated with achieving high cooling rate through rapid extraction of thermal energy (superheat and latent heat of fusion).[4,5] Among the available techniques that may be effectively used to enhance the degree of undercooling during solidification, atomization remains a popular choice as a result of its versatility and potential for tonnage production.[6] For example, a single atomization experiment may be used to generate a wide range of powder sizes with concomitant variation in solidification conditions.[7–9] Control of the amount of undercooling prior (i.e., controlling particle size) to solidification may be effectively utilized to promote the formation of nonequilibrium phases as highly refined microstructures with concomitant benefits for mechanical behavior. Increasing the extent undercooling may expand the range of available phases by allowing competitive nucleation and growth.[1–5,10] Accordingly, an understanding of the factors that control the extent of undercooling may be helpful to tailor the microstructure.

The Al–Fe system is of interest for several reasons: (i) when solidified in the presence of a high undercooling, this system forms several dispersoids of the Al_mFe type[11–13]; (ii) this system constitutes the basis of a family of commercially important elevated temperature Al alloys due to the very low equilibrium solid solubility and very low diffusion rate of Fe in Al.[14,15] The microstructure and phase stability of Al–Fe alloys are strongly influenced by the extent of undercooling during solidification[16–18] as well as by the concentration of Fe.[19] For example, under identical solidification conditions lowering the Fe content can result in a more homogeneous microstructure and finer primary Al_mFe particles.[19]

In addition, the content of Fe has an effect on the relative stability of metastable Al_6Fe phase and stable Al_3Fe phase[20] (now known to be $Al_{13}Fe_4$). It has been well documented[16–18,20,21] that two distinct types of microstructure coexist in Al–Fe powders, which have been designated as Zone A and Zone B, respectively. Zone A represents a microeutetic or microcellular structure, whereas Zone B represents a dendritic structure. Moreover, the presence of a high undercooling can suppress or, at least reduce, the formation of some primary phases.[22] Therefore, the objective of the present investigation was to enhance the understanding

of the effect of solidification condition on the resultant microstructure and phase stability of Al–Fe alloys.

II. EXPERIMENTAL

Two alloys with nominal composition of Al–2.56 wt% Fe and Al–6.0 wt% Fe were selected for this study. The alloys were prepared by using pure Al (99.99%) and Fe (99.98%). In the atomization experiment, the alloys were first superheated to temperatures of 200 K above the equilibrium liquidus and atomized into a distribution of droplets by using nitrogen gas.

To reduce oxidation, the experiments were conducted inside an environmental chamber, which was evacuated down to a pressure of 100 Pa and backfilled with nitrogen to a pressure of 1.05×10^5 Pa prior to melting and atomization. The primary atomization variables used in the present study are listed in Table I.

The atomized Al–Fe powders were collected and their size distribution were established by mechanical sieving according to ASTM standard B214. The powders were then mounted for microstructural analyses using standard metallographic techniques and etched with Keller's reagent in order to reveal microstructural features.

The phases that were present in the powders were identified by x-ray diffractometry. The x-ray measurements were conducted in a Siemens D5000 diffractometer using Cu $K_{\alpha 1}$ radiation with a wavelength $\lambda = 1.5406$ Å. X-ray diffraction spectra were determined in the $2\theta = 10°$ to $2\theta = 130°$ range with a resolution of 0.02° and a time step of 2 s. Characterization of the morphology of the various phases present and microanalysis of the Fe content in specific phases were conducted using a scanning electron microscope (SEM). The SEM studies were also carried out to measure the secondary dendrite arm spacing (SDAS) in the atomized powders.

III. RESULTS AND DISCUSSION

The size distribution of Al–2.56 wt% Fe and Al–6.0 wt% Fe powders were established by summarizing the results of the sieving experiments in a probability graph of cumulative weight percentage versus powder diameter. The results summarized in Fig. 1 suggest that the size distribution of the atomized powders may be approximated by a logarithmic-normal function. Based on a logarithmic-normal relationship, a mass median powder diameter d_{50} was determined to be 109 μm for the Al–2.56 wt% alloy and 85 μm for the Al–6.0 wt% Fe alloy, respectively. The specific powder sizes, d_{16} and d_{84}, which corresponded to the opening of a screen mesh which lets through 16 and 84 wt% of the powders, respectively,[23] were also determined and summarized in Table I.

TABLE I. Experimental variables and specific diameters of atomized powders.

Variables	Values	
Material (wt%)	Al–2Fe	Al–6Fe
Superheat temperature (K)	1053	1143
Atomization gas	N_2	N_2
Atomization gas pressure (MPa)	1.55	1.97
Gas flow rate (kg/s)	0.024	0.029
Metal flow rate (kg/s)	0.028	0.029
d_{16} (μm)	46	34
d_{50} (μm)	109	85
d_{84} (μm)	263	232

Results obtained from metallographic studies in the as-atomized Al–2.56 wt% Fe and Al–6.0 wt% Fe powders revealed the following kind of microstructures. The as-atomized microstructure of Al–2.56 wt% Fe consisted in droplets with sizes in the range between 10 and 40 μm in diameter showing dendritic domains and some of them exhibited a predendritic feature. Figure 2 shows a dendritic domain which present the development of regular dendritic growth from an initially predendritic mode.

The distribution of solute (Fe) in the predendritic region as shown by scanning electron microscopic analyses is given in Table II. The weight percent Fe in single phase (a) was within experimental limits, the same as the parent melt. In region (b) the Fe content showed a minimum, and in region (c), before cells or dendrites start to form, the average composition was again that of the liquid. This predendritic formation was identified by Biloni and Chalmers,[24] in chill-casted Al–Cu alloys and also reported in Al–Mn alloys[25] and were identified on the side of the ingot which was in direct contact with a chill-copper wall. These morphologies show the extreme condition of solid solubility extension which occurs when solidification occurs effectively without

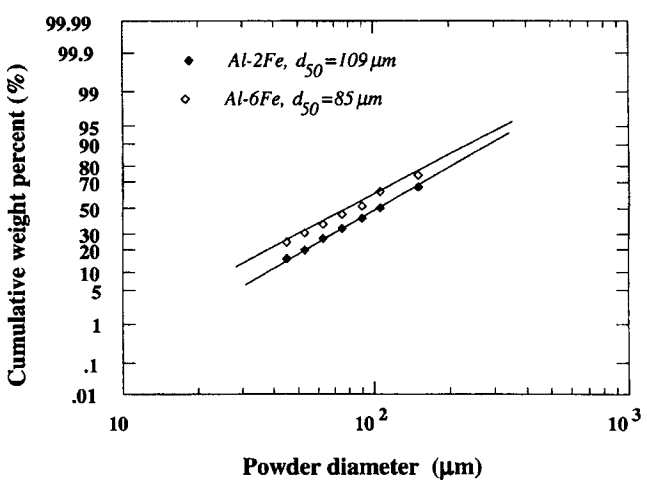

FIG. 1. Size distribution of atomized Al–Fe powders.

TABLE II. SEM microanalyses (in wt% Fe) carried out in powders of Fig. 2.

Microanalysis	Region A	Region B	Region C	Dendrites
Center	2.56 ± 0.09		2.56 ± 0.09	
1 μm from center	2.56 ± 0.05			
Region B		2.52 ± 0.10		
Near region C				2.54 ± 0.12
5 μm far from Region C				2.49 ± 0.10
Close to grain boundary				2.45 ± 0.09

solute partitioning to give a single-phase solid of uniform composition, C_0, the same as the parent melt. SEM observations of predendritic zones suggest that regions such as (a) and (c) of high solute content were the first regions where nucleation occurred and from which growth occurred initially with a smooth spherical front without net segregation.

Thermodynamic explanation of this diffusionless solidification suggest that this solidification without change in composition should be possible at temperatures below the temperature at which both solid and liquid of a given composition have the same free energy and is the maximum temperature for nonpartitioning, diffusionless, or massive solidification, for the composition involved (i.e., T_0 curve; see Fig. 3). Predendritic formation as is shown in Fig. 2 is limited by stability of the solidification front toward perturbation, leading to cellular or dendritic growth accompanied by solute partitioning, concentration gradients in the solid, and finally intercellular or interdendritic separation of a second phase beyond region (c).

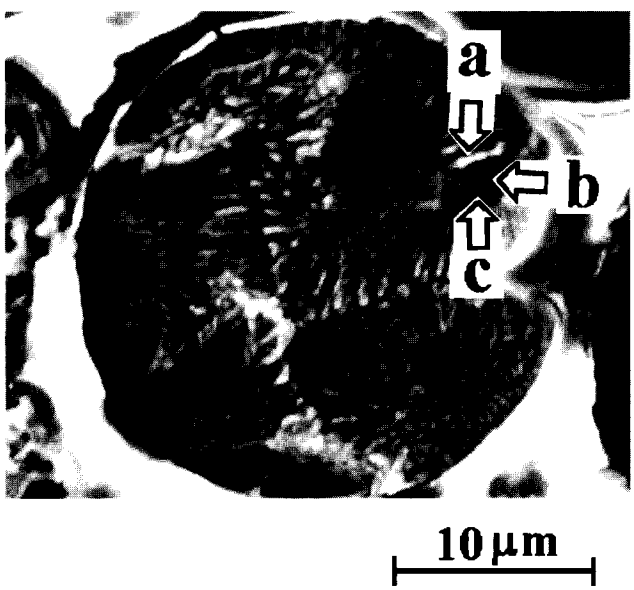

FIG. 2. Atomized powder particle observed in Al–2.56 wt% Fe alloy in which a predendritic microstructure is observed. The wt% Fe in single phase *a* and *c* was the same as the parent melt and position *b* a minimum.

Figure 4(a) shows another microstructure observed in Al–2.56 wt% Fe powders in the size range between 20 and 50 μm in diameter. This microstructure is similar to that reported by Boettinger *et al.*,[16] in which the bottom left size of the powder exhibited a primarily microcellular [marked with the letter (a) in Fig. 4(a)] fcc α–Al solid solution which suggests that nucleation appears to have occurred at a single site on the surface of the particle and the solidification front passes from left to right, but the advancing of the solidification front was not as high as the above microstructure (predendritic), leading to segregation at cell boundaries. As solidification front velocity decreases, the structure of atomized powders of the Al–2.56 wt% Fe passes from the predendritic (Fig. 2), microcellular [Fig. 4(a)] to a cellular [Fig. 4(b)] or dendritic one [Fig. 4(c)]. Observe that in these particle sizes and for this particular composition, the presence of Al_3Fe or Al_6Fe as primary intermetallic was not detected.

For the Al–6.0 wt% Fe powders, apart from the cellular or dendritic structure, it was observed in powders particles with sizes > 50 μm, the presence of primary phases which were generally plate-like or blocky [Fig. 5(a)]; this observation is consistent with the studies on rapidly solidified Al–Fe alloys[16–19,26] in which this primary phase was identified as the intermetallic Al_3Fe. Another kind of observed microstructure was that which

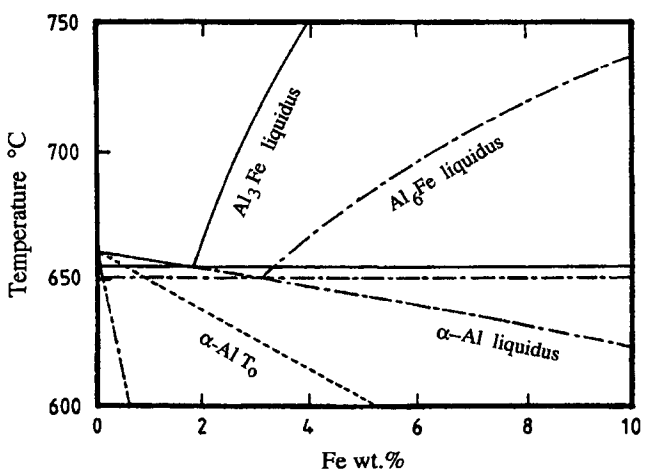

FIG. 3. Al-rich side of the binary Al–Fe nonequilibrium phase diagram, calculated by Murray.[34]

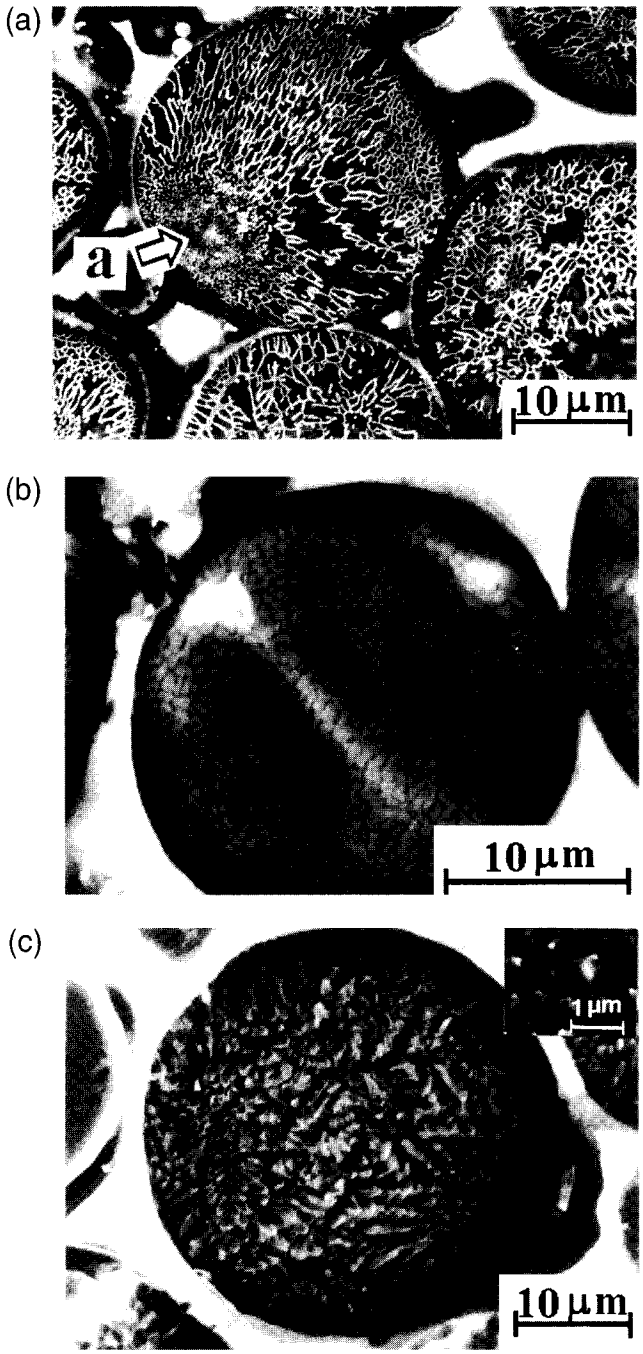

FIG. 4. Different morphologies observed in Al–2.56 wt% Al alloy powders. (a) Microcellular fcc α–Al solid solution, (b) cellular α–Al solid solution, and (c) dendritic α–Al solid solution; inset shows dendritic tip morphology.

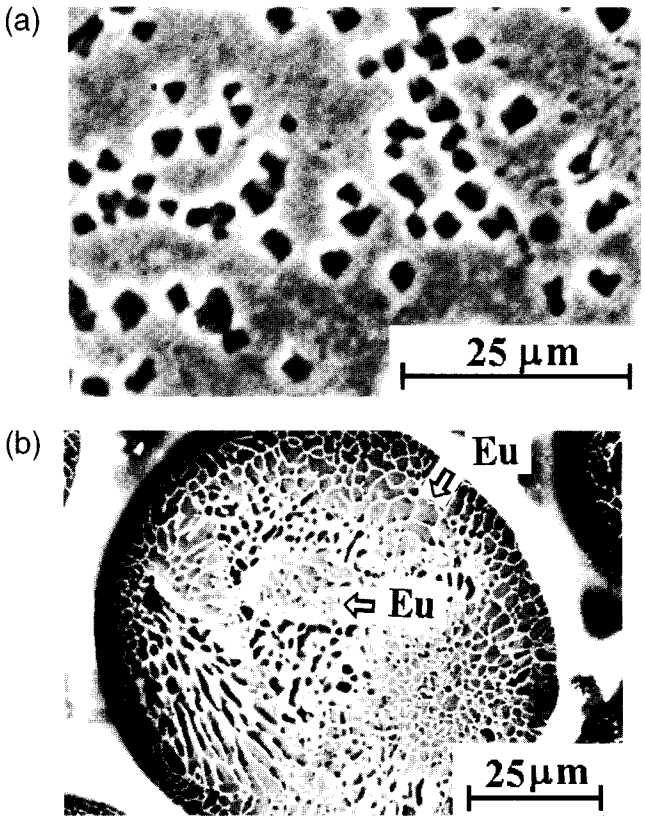

FIG. 5. (a) Primary intermetallic Fe_3Al and (b) eutectic α–A-Al + Al_6Fe observed in Al–6 wt%. Fe alloy powders with sizes > 50 μm.

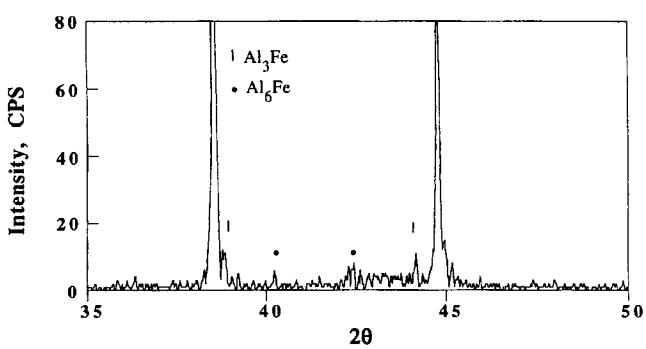

FIG. 6. X-ray spectra of atomized Fe–6 wt% Fe powders in the size range of 45 to 53 μm; the strong diffraction peaks are from matrix α–Al phase; the weak diffraction peaks from Al_3Fe and Al_6Fe are indicated in the figure.

exhibited an eutectic morphology of α–Al + Al_6Fe as is shown in Fig. 5(b). The phases that were present in the atomized Al–6.0 wt% Fe were further identified by x-ray diffraction analysis; according to the x-ray diffraction spectra (Fig. 6), the strong peaks were those corresponding to the α–Al phase, whereas the relatively weak diffraction peaks were from the intermetallic Al_3Fe and Al_6Fe.

Table III summarizes the measured Fe contents in the α–Al phase as determined for Al–2.56 wt% Fe and Al–6.0 wt% Fe powders of different powder sizes (35, 55, and 90 μm) using SEM microanalysis. This table shows that for Al–2.56 wt% Fe and Al–6.0 wt% Fe powders, the content of Fe in α–Al phase increases with decreasing powder size as reported in several works.[27,28] It has been documented[29] that the

TABLE III. Measured Fe content (wt%) in α–Al phase by using SEM microanalysis.

Al–2.56 wt% Fe			Al–6.0 wt% Fe		
90 μm	55 μm	33 μm	90 μm	55 μm	33 μm
2.21 ± 0.12	2.38 ± 0.11	2.56 ± 0.09	5.71 ± 0.025	5.76 ± 0.030	5.98 ± 0.10

maximum solid solubility of Fe in Al at equilibrium is 0.025 at. %. In the present study, the SEM microanalysis results (Table III) demonstrated that the solubility of Fe in the α–Al phase can be extended significantly under the investigated solidification conditions. It is noteworthy that the content of Fe in the α–Al phase measured is very close to the designated alloy composition, suggesting that solute trapping may have occurred under the current experimental conditions. As discussed in Ref. 30, one of the characteristics of rapid solidification is the attainment of relatively high levels of undercooling prior to the onset of nucleation. Atomization may be used to attain high levels of undercooling while simultaneously promoting rapid rates of thermal energy transfer and thereby high cooling rates. These conditions are typically used to rationalize the presence of a refined solidification morphology (i.e., small SDAS) and the formation of nonequilibrium microstructures (i.e., extended solid solution) that are commonly reported for atomized powders. To a certain extent, processing variables can be manipulated to control the degree of undercooling and thereby promote a transition in solidification microstructural features.

The formation of various phases during atomization may be further understood on the basis of a competitive nucleation mechanism. Perepezko[31] and Bosewell and Chadwick[32] elucidated how an increased cooling rate might be expected to enhance the attainment of high undercooling before nucleation of different phases by using time-temperature-transformation curves. For the present Al–Fe powders, the formation of different phases may further be rationalized using a metastable phase diagram such as that shown in Fig. 3, which shows the Al-rich side of the binary Al–Fe phase diagram which includes the metastable phase boundary and α–Al lines as calculated by Murray.[33] The phase diagram indicates that the formation of a range of metastable phases and microstructural morphologies depends on the degree of initial undercooling experienced by the powders. The relative amount of these phases, however, may also be affected by their growth kinetics. For example, it has been shown that at high solid/liquid interface growth velocities, the Al_6Fe phase is favored in suppression of the Al_3Fe phase and the minimum growth velocity necessary for suppression of the Al_3Fe phase increases with Fe content.[34,35]

On the other hand, in order to explain the formation of the observed predendritic, cellular, and/or dendritic structures, predictions of rapid dendrite growth in undercooled alloys were calculated according to the theory of dendrite growth into undercooled alloy melts for the case of large undercoolings, reported by Lipton *et al.*,[36] where a complete stability analysis of a plane interface to the tip of a Ivantsov dendrite was considered. The dendrite growth problem was defined,[36] assuming a simplified isolated dendrite tip of the form described by a paraboloid of revolution,[37] growing with a constant dimensionless growth rate, $\overline{V}$, and dimensionless tip radius, $\overline{R}$, into the bath with a given dimensionless undercooling, $\overline{\Delta T}$, defined by Eqs. (1)–(3):

$$\overline{\Delta T} = Iv(P_t) + \overline{Co}(A - 1)^{-1} + 2\sigma^* P_t F(A), \quad (1)$$

$$\overline{R} = [\sigma^* P_t F(A)]^{-1}, \quad (2)$$

$$\overline{V} = \sigma^* P_t^2 F(A), \quad (3)$$

The parameters fed into the mathematical model are shown in Table IV, for the Al–Fe system under study and the list of symbols in Table V.

Results of Eqs. (1)–(3) are plotted in Fig. 7 showing the behavior of $\overline{V}$ and $\overline{R}$ as a function of $\overline{\Delta T}$ [Figs. 7(a) and 7(b)], respectively, for $\overline{Co} = 0.02$, $k_0 = 0.038$, and $\eta = 1.41 \times 10^{-4}$. According to that figure, the behavior of $\overline{V}$ as a function of $\overline{\Delta T}$ and $\overline{R}$ as a function of $\overline{\Delta T}$ (also the plots of ξ as a function of $\overline{\Delta T}$ and P as a function of $\overline{\Delta T}$, and not included here) was similar to those reported by Lipton *et al.*[38] In particular, it can be observed that at high undercoolings, the dimensionless tip radius shows a minimum ($\overline{R} \approx 10$, $\overline{\Delta T} \approx 0.58$) followed by a maximum ($\overline{R} \approx 153$, $\overline{\Delta T} \approx 0.85$) before going to infinity and $\overline{V}$ approaches a maximum value close to 0.5. The complex behavior of $\overline{R}$ as a function of $\overline{\Delta T}$ was explained by Lipton *et al.*[38] as a change from an almost purely solute diffusion controlled dendrite growth [minimum in Fig. 7(b)] to a thermal plus solutal control [maximum in Fig. 7(b)].

With regards to the microstructure observed in nitrogen atomized Al–Fe powders and in particular those presented in Figs. 2 and 4(c), it can be mentioned that those two atomized particles represent the main morphologies observed in the powders. Figure 4(c) shows a powder particle in which it can be observed a dendrite solidification growth mode and its dendrite tip (inset) adopting a form closely described by a paraboloid of revolution. Assuming that this dendrite tip grew with

TABLE IV. Parameters fed into the mathematical model.

Unit undercooling	$\theta = H/c_p$	368.7 (K)
Capillarity length	$d_0 = \Gamma/\theta$	2.71×10^{-10} (m)
Ratio thermal/solutal diffusivity	$\eta = \alpha/D$	1.41×10^4 (···)
Alloy concentration	$C_0 = \overline{Co}\theta/\lvert m\rvert$	99.6 $\overline{Co}$ (wt%)
Bath undercooling	$\Delta T = \theta\overline{\Delta T}$	368.7 $\overline{\Delta T}$ (K)
Growth rate	$V = 2a\overline{V}/d_0$	2.51×10^5 $\overline{V}$ (m/s)
Dendrite tip radius	$R = \overline{R}d_0$	2.71×10^{-10} $\overline{R}$ (m)
Liquidus slope	m	−3.7 (k/wt%)
Equilibrium partition coefficient	k_0	0.038 (···)

a constant $\overline{V}$ and $\overline{R}$ into the bath with a given undercooling, then the observed dendrites in the powder particle grew at some point positioned to the left of the coordinate point $(\overline{\Delta T}_3, \overline{R}_3)$ shown in Fig. 7(b).

This kind of morphology has already been reported,[16] and its formation has been explained in terms of interface movement at a velocity nearly constant across the entire droplet to form a mixture of liquid and solid at the end of recalescence with a dimensionless undercooling of the form $\Delta\theta = \Delta T/(L/C) < 1$ (where ΔT is the initial undercooling below the relevant liquidus temperature, L the latent heat per unit volume, and C the liquid heat capacity per unit volume); later the interdendritic regions solidify by removal of latent heat to the powder exterior usually at a much lower rate.

TABLE V. List of symbols.

A	Ratio of tip to initial alloy concentration = $[1-(1-k_0)Iv(P_c)]^{-1}$
α	Thermal diffusivity (m^2/s)
$\overline{Co}$	Dimensionless alloy concentration = $C_0\lvert m\rvert/\theta$
C_0	Alloy concentration (wt%)
c_p	Heat capacity of liquid (J/m^3K)
d_0	Capillarity length = Γ/θ (m)
D	Solute diffusion coefficient (m^2/s)
$F(A)$	Stability function = $\xi_t + \xi_c 2\eta\overline{Co}\,A(1-k_0)$
$Iv(P)$	Ivantsov function = $P\exp(P)E_1(P)$ with $E_1(P)$ the exponential integral function, where P is the solutal or thermal Péclet number
H	Volumetric latent heat of fusion (J/m^3)
k_0	Equilibrium partition coefficient
P_c	Solutal Péclet number = $VR/2D$
P_t	Thermal Péclet number = $VR/2a$
$\overline{R}$	Dimensionless dendrite tip radius = R/d_0
$\overline{V}$	Dimensionless growth rate = $Vd_0/2\alpha$
Γ	Gibbs–Thomson parameter = $\sigma T_f/H$ (Km)
m	Slope of liquidus line (K/wt%)
η	Ratio of thermal/solutal diffusivity = a/D
θ	unit undercooling = H/c_p (K)
ξ_c	Solutal stability parameter
ξ_t	Thermal solubility parameter
σ	Solid/liquid interface energy (J/m^2)
σ^*	Stability constant $[1/(4\pi^2)]$

Identification of symbols

In	$[1-(1-k_0)Iv(P_c)]^{-1}$	1 = one and 0 = zero
In	$\overline{Co}$	o = zero
In	$C_0\lvert m\rvert/\theta$	0 = zero
In	C_0	0 = zero
In	d_0	0 = zero
In	$Iv(P_t) + \overline{Co}(A-1)^{-1} + 2\sigma^* P_t F(A)$	0 = zero and 1 = one
In	$[\sigma^* P_t F(A)]^{-1}$	1 = one

Figure 2 shows the second kind of morphology observed in the atomized powders. These powders show the following characteristics: (i) a circle was observed which did not show any kind of features; (ii) this circle [marked with (a)] was surrounded by a concentric ring which also did not show any features [marked with (c)]; (iii) from the outside of this concentric ring, dendrites started to grow; (iv) dendrites continue to grow and increase in dimensions (i.e., tip radius and primary dendrite spacing increase); and (v) the growing of dendrites stop at grain boundaries.

Observing the behavior of Fig. 7(b) and analyzing it from low to high values of $\overline{\Delta T}$, with respect to the microstructural features of Fig. 2(a), it can be pointed out that the dendrite tip radius, R, of dendrites observed close to the grain boundary ($R \approx 0.2$ μm) will decrease in dimension as $\overline{\Delta T}$ and $\overline{V}$ increase until those parameters force that $\overline{R}$ reaches a minimum value in the plot of $\overline{\Delta T}$ versus $\overline{R}$ ($\overline{\Delta T} \approx 0.58$, $\overline{R} \approx 10$, and $R \approx 0.01$ μm, with $d_0 = 3.33 \times 10^{-10}$ m). This minimum in $\overline{R}$ of Fig. 8(b) will correspond to the interface dendrite/concentric ring (marked with C) in Fig. 2(a). In that interface $R \approx 0.05$ μm, which is close to the value of R determined from the plot of $\overline{\Delta T}$ versus $\overline{R}$ ($R \approx 0.01$ μm). The maximum in $\overline{R}$ from that plot and located as a coordinate point $(\overline{\Delta T}_2, \overline{R}_2)$ will correspond to the interface concentric ring/circle of Fig. 2(a). And finally, the circle of Fig. 2(a) correspond to the portion of the plot of $\overline{\Delta T}$ versus $\overline{R}$ when the value of $\overline{R}$ goes to infinity.

In terms of microstructure, the circle will correspond to a region in which formation of a segregation-free microstructure occurred. This microsegregation-free microstructure will result as the product of rapid solidification from the melt under kinetic conditions that give

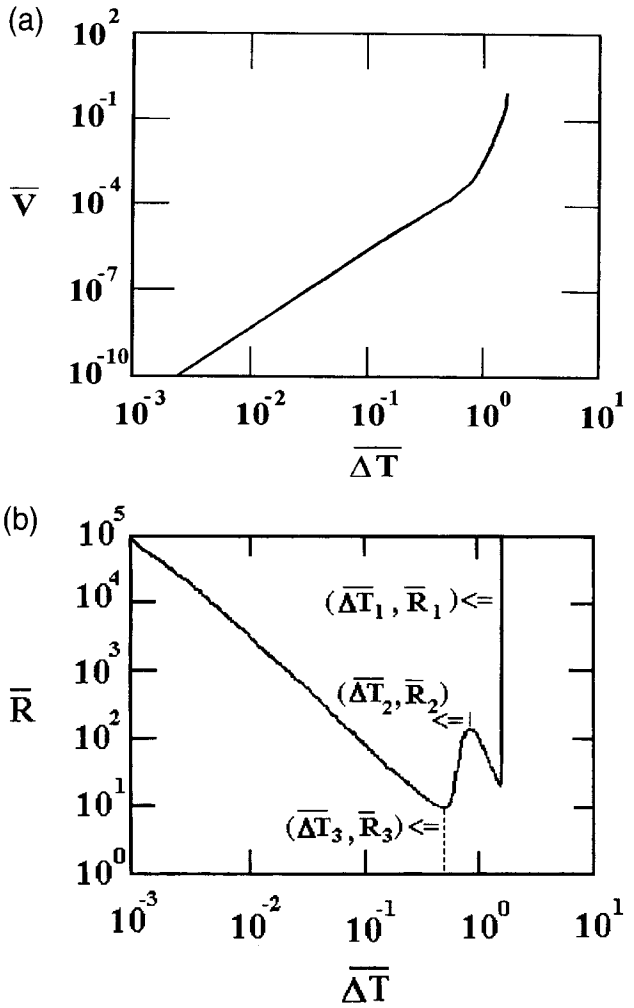

FIG. 7. (a,b) Behavior of $\overline{V}$ and $\overline{R}$ as a function of $\overline{\Delta T}$, respectively, for $\overline{Co} = 0.02$, $k_0 = 0.038$, and $\eta = 1.41 \times 10^{-4}$. In particular, it can be observed that at high undercoolings, the dimensionless tip radius shows a minimum ($\overline{R} \approx 10$, $\overline{\Delta T} \approx 0.58$) followed by a maximum ($\overline{R} \approx 153$, $\overline{\Delta T} \approx 0.85$) before going to infinity and $\overline{V}$ approaches to a maximum value close to 0.5. The coordinate points $(\overline{\Delta T}_3, \overline{R}_3)$, $(\overline{\Delta T}_2, \overline{R}_2)$, and $(\overline{\Delta T}_1, \overline{R}_1)$ show the position of $\overline{R}$ in the curve which correspond to a minimum, maximum, and infinity, respectively.

rise to absolute stability of the advancing solidification front against perturbations or that lead to trapping of solute in the solid. As reported by Jones,[39] formation of a segregation-free α–Al solid solution for the Al–Fe system is expected to be governed by solute trapping essentially at all concentrations (the velocity needed for absolute stability, $V_a \approx 151$ m/s for an alloy composition of 2.56 wt% Fe). Therefore, when the plot of $\overline{\Delta T}$ versus $\overline{R}$ goes to infinity indicates formation of a segregation-free solid due to trapping of solute in the solid. When a maximum in $\overline{R}$ is observed in the plot of $\overline{\Delta T}$ versus $\overline{R}$ of Fig. 7(b), it will be assumed that this behavior corresponds to a perturbation of the system, as that presented in the interface circle/concentric ring, which gives place to the growth of cells or dendrites, as is observed schematically in Fig. 2(a) at the interface concentric ring/dendrites.

IV. CONCLUDING REMARKS

In the present study, four types of microstructure in the atomized Al–Fe powders were found, Al_3Fe phase, Al + Al_6Fe eutectic, α–Al dendrite, and a predendrite structure. SEM microanalysis demonstrated that the Fe content in α–Al phase increases with decreasing powder size.

The model of Lipton *et al.*[38] for rapid dendrite growth in undercooled alloys was applied to the rapid solidification of nitrogen-atomized Al–2.56 wt% Fe alloy powders. The outcome of the model in terms of $\overline{\Delta T}$ versus $\overline{V}$ and $\overline{\Delta T}$ versus $\overline{R}$ showed a similar behavior as those reported by the above authors.

The plot of $\overline{\Delta T}$ versus $\overline{R}$ can be explained in terms of the microstructure observed in the atomized powders as (i) a region which shows an interface concentric ring/dendrites and correspond to the minimum in the plot of $\overline{\Delta T}$ versus $\overline{R}$; from this minimum (interface) dendrites start to growth and stop at grain boundary; (ii) a region which shows an interface circle/concentric ring and corresponds to a maximum in the plot of $\overline{\Delta T}$ versus $\overline{R}$; dendrites are not longer observed and the solute content is the same as the parent melt; and (iii) a region of a circle which correspond to the portion of the plot of $\overline{\Delta T}$ versus $\overline{R}$ when $\overline{R}$ goes to infinity. Regions of circle and concentric ring are regions where a segregation-free solid is formed due to the trapping of solute in the solid.

ACKNOWLEDGMENTS

Support from NASA under Grant No. NAGI-1619 and NSF INT-9600517 are gratefully acknowledged. The authors would like to thank Dr. Y. Wu and Dr. X. Liang for insightful discussions as well as contributions to the experimental work, and Mr. E. A. Caballero-Rodriguez for his technical support.

REFERENCES

1. D. Turnbull, in *Undercooled Alloy Phases*, edited by E. W. Collings and C. C. Koch (AIME-TMS, Warrendale, PA, 1987), pp. 3–22.
2. J. H. Perepezko, B. A. Mueller, and K. Ohsaka, in *Undercooled Alloy Phases*, edited by E. W. Collings and C. C. Koch (AIME-TMS, Warrendale, PA, 1987), pp. 298–320.
3. M. C. Flemings, Y. Shiohara, Y. Wu, and T. J. Piccone, in *Undercooled Alloy Phases*, edited by E. W. Collings and C. C. Koch (AIME-TMS, Warrendale, PA, 1987), pp. 321–343.
4. A. J. Drehman and D. Turnbull, Scripta Metall. **15**, 543 (1981).
5. Y. E. Anderson and M. P. Kemppainen, in *Undercooled Alloy Phases*, edited by E. W. Collings and C. C. Koch (AIME-TMS, Warrendale, PA, 1987), pp. 269–285.

6. A. Lawley, in *Processing of Structural Metals by Rapid Solidification*, edited by F. H. Froes and J. S. Savage (ASM INTERNATIONAL, Metals Park, OH, 1987), pp. 31–40.
7. H. Jones, in *Rapid Solidification Processing: Principles and Technology*, edited by R. Meharabian, B. H. Kear, and M. Cohen (Claitor's Publishing Division, 1978), pp. 28–45.
8. N. J. Grant, in *Rapid Solidification Processing: Principles and Technology*, edited by R. Mehrabian, B. H. Kear, and M. Cohen (Claitor's Publishing Division, 1978), pp. 230–245.
9. E. J. Lavernia, J. D. Ayers, and T. S. Srivatsan, Int. Mater. Rev. **37**, 1 (1992).
10. W. J. Boettinger, in *Rapidly Solidified Amorphous and Crystalline Alloys*, edited by B. H. Kear, B. C. Giessen, and M. Cohen (Mater. Res. Soc. Symp. Proc. **8**, Elsevier Science Publishing, New York, 1982), pp. 15–31.
11. D. J. Skinner, K. Okazaki, and C. M. Adam, in *Rapidly Solidified Powder Aluminum Alloys*, edited by M. E. Fine and E. A. Starke, Jr. (ASTM-STP 890, Philadelphia, PA, 1986), pp. 211–236.
12. M. J. Couper and R. F. Singer, in *High Strength Powder Metallurgy Aluminum Alloys II*, edited by G. J. Hildeman and M. J. Kpczak (AIME-TMS, Warrendale, PA, 1986), pp. 199–211.
13. W. G. J. Bunk, Mater. Sci. Eng. **A134**, 1087 (1991).
14. C. Suryanarayana, F. H. Froes, and W. E. Quist, in *Advances in Powder Metallurgy, 1991* (American Powder Metallurgy Federation, 1991), Vol. 6, pp. 15–29.
15. P. S. Gilman, R. G. Rateick, and A. Testa, in *Advances in Powder Metallurgy, 1991* (American Powder Metallurgy Federation, 1991), Vol. 6, pp. 47–57.
16. W. J. Boettinger, L. Bendersky, and J. G. Early, Metall. Trans. **17A**, 781 (1986).
17. R. F. Cochrane, P. V. Evans, and A. L. Greer, Mater. Sci. Eng. **A133**, 803 (1991).
18. R. F. Cochrane, S. B. Newcomb, P. V. Evans, and A. L. Greer, Key Engineering Mater. **38 & 39**, 21 (1989).
19. J. D. Cotton and M. J. Kaufman, Metall. Trans. **22A**, 927 (1991).
20. C. M. Adam, in *Rapidly Solidified Amorphous and Crystalline Alloys*, edited by B. H. Kear, B. C. Giessen, and M. Cohen (Elsevier, New York, 1982), pp. 411–422.
21. H. Jones, Mater. Sci. Eng. **5**, 1 (1969).
22. J. H. Perepezko, J. A. Graves, and B. A. Mueller, in *Processing of Structural Metals by Rapid Solidification*, edited by F. H. Froes and S. J. Savage (ASM INTERNATIONAL, Metals Park, OH, 1987), pp. 13–29.
23. E. J. Lavernia, T. S. Srivatsan, and R. H. Rangel, Atomization and Sprays **2**, 253 (1992).
24. H. Biloni and B. Chalmers, Trans. Metall. Soc. AIME **233**, 373 (1965).
25. J. A. Juarez-Islas, Ph. D. Thesis, University of Sheffield, England (1987), p. 35.
26. T. Turmezey, V. Stefaniay, and A. Griger, Key Engineering Mater. **38 & 39**, 43 (1989).
27. C. M. Adam and L. M. Hogan, J. Australian Inst. Metals **17**, 81 (1972).
28. Y. R. Hughes and H. Jones, J. Mater. Sci. **11**, 1781 (1976).
29. H. Jones, Philos. Mag. B **61**, 487 (1990).
30. H. Jones, *Rapid Solidification of Metal and Alloys* (Institution of Metallurgists, London, 1982), p. 35.
31. J. H. Perepezko, in *Science and Technology of the Undercooled Melts*, edited by P. R. Sahm, H. Jones, and C. M. Adam (Martinus Nijhoff Publishers, 1986), pp. 29–52.
32. P. G. Boswell and G. A. Chadwick, J. Mater. Sci. **12**, 1879 (1977).
33. P. G. Keong, J. A. Sames, C. M. Adam, and R. H. Sharo, in *Rapid Solidification and Casting of Metals* (The Metals Society, 1979), pp. 110–114.
34. J. L. Murray, in *Alloy Phase Diagrams*, edited by L. H. Bennett, T. B. Massalski, and B. C. Giessen (Mater. Res. Soc. Symp. Proc. **19**, Elsevier Publishing Co., New York, 1983), pp. 249–262.
35. C. M. Adam and L. M. Hogan, J. Australian Inst. Metals **17** (2), 81 (1972).
36. J. Lipton, W. Kurz, and R. Trivedi, Acta Metall. **35**, 957 (1987).
37. G. P. Ivantsov, Dokl. Akad. Nauk SSSR **58**, 567 (1947).
38. J. Lipton, M. E. Glicksman, and W. Kurz, Mater. Sci. Eng. **64**, 57 (1984).
39. H. Jones, Mater. Lett. **6**, 181 (1988).